A&A, 687, A56 (2024)
https://doi.org/10.1051/0004-6361/202348832

Astronomy & Astrophysics

AMICO-COSMOS galaxy cluster and group catalogue up to $z = 2$: Sample properties and X-ray counterparts⋆

G. Toni[1,2,3], M. Maturi[3,4], A. Finoguenov[5], L. Moscardini[1,2,6], and G. Castignani[1,2]

[1] Dipartimento di Fisica e Astronomia "A. Righi", Alma Mater Studiorum Università di Bologna, Via Gobetti 93/2, 40129 Bologna, Italy
e-mail: greta.toni4@unibo.it
[2] INAF – Osservatorio di Astrofisica e Scienza dello Spazio di Bologna, Via Gobetti 93/3, 40129 Bologna, Italy
[3] Zentrum für Astronomie, Universität Heidelberg, Philosophenweg 12, 69120 Heidelberg, Germany
[4] ITP, Universität Heidelberg, Philosophenweg 16, 69120 Heidelberg, Germany
[5] Department of Physics, University of Helsinki, Gustaf Hällströmin katu, 2, 00560 Helsinki, Finland
[6] INFN – Sezione di Bologna, Viale Berti Pichat 6/2, 40127 Bologna, Italy

Received 4 December 2023 / Accepted 5 March 2024

ABSTRACT

Aims. We present the results of a new galaxy cluster search in the COSMOS field obtained using the Adaptive Matched Identifier of Clustered Objects (AMICO). Our aim was to produce a new cluster and group catalogue up to $z = 2$ by performing an innovative application of AMICO with respect to previous successful applications to wide-field surveys in terms of depth (down to $r < 26.7$), small area covered ($\sim$1.69 deg^2 of unmasked effective area), and redshift extent. This sample and the comparative analysis we performed with the X-rays, allowed for the calibration of mass-proxy scaling relations up to $z = 2$ and down to less than 10^{13} $M_\odot$, and constitutes the basis for the refinement of the cluster model for future applications of AMICO, such as the analysis of upcoming *Euclid* data.
Methods. The AMICO algorithm is based on an optimal linear matched filter and detects clusters in photometric galaxy catalogues using galaxy location, photometric redshift and, in the simplest case, one galaxy property. We chose to use a single magnitude as the galaxy property, avoiding the explicit use of galaxy colour for the selection of clusters. We used three different magnitudes by performing three independent runs in the r-, Y-, and H-bands using both COSMOS2020 and COSMOS2015 galaxy catalogues. We created a composite visibility mask and cluster models for the signal to detect, and we estimated the noise directly from the data.
Results. We performed a matching of the catalogues resulting from the three runs and merged them to produce a final catalogue that contains 1269 and 666 candidate clusters and groups with $S/N > 3.0$ and >3.5, respectively. A total of 490 candidates are detected in all three runs. Most of the detections unmatched between runs have $S/N < 3.5$, which can be set as a threshold for selecting a more robust sample. We assigned X-ray properties to our detections by matching the catalogue with a public X-ray selected group sample and by estimating, for unmatched detections, the X-ray properties at the location of AMICO candidates using *Chandra+XMM-Newton* data. There are in total 622 candidate clusters and groups with an X-ray flux estimate. This large sample of candidates with X-ray properties allowed the calibration of the scaling relations between two AMICO mass-proxies (richness and cluster amplitude) and X-ray mass and the study of their redshift dependence for the selection of the most stable photometric bands.

Key words. galaxies: clusters: general – galaxies: evolution – galaxies: groups: general – galaxies: luminosity function, mass function

1. Introduction

Clusters of galaxies are established tracers of density peaks in the large-scale matter distribution and have proven to be a powerful probe of cosmology (see Allen et al. 2011, for a review). They can be used to constrain cosmological parameters through number density (e.g. Rosati et al. 2002; Vikhlinin et al. 2009; Rozo et al. 2010; Costanzi et al. 2019; Lesci et al. 2022a) and spatial distribution (e.g. Veropalumbo et al. 2014; Marulli et al. 2018; To et al. 2021; Lesci et al. 2022b; Romanello et al. 2024). Additionally, galaxy clusters are important laboratories for the study of astrophysical processes, such as those underlying galaxy formation and evolution. Clusters and groups as galactic environments influence the development of galaxy properties, as proven by the observed differences between field galaxies and galaxies in denser environments (e.g. Dressler 1980; Kuchner et al. 2017; George et al. 2011). The understanding of galaxy cluster astrophysics is also fundamental so they can be used as cosmological probes. A reliable method for the identification of clusters and the determination of the mass-observable relation linking the cluster masses to direct observables is a crucial requirement for the cosmological exploitation of galaxy clusters (e.g. Pratt et al. 2019; Singh et al. 2020).

Galaxy clusters can be detected from the hot gas that the galaxies are embedded in, which makes them bright X-ray sources (e.g. Böhringer et al. 2004; Finoguenov et al. 2010) and leaves an imprint at millimetre wavelengths by distorting the cosmic microwave background (CMB) spectrum (the thermal Sunyaev Zeldovich effect or SZ, Sunyaev & Zeldovich 1970; e.g. Bleem et al. 2015; Hilton et al. 2018). In the optical and near-infrared (NIR) clusters can be detected via the gravitational lensing of background sources (e.g. Maturi et al. 2005; Stapelberg et al. 2019; Hamana et al. 2020) and through the properties of member galaxies. Photometric catalogues of

⋆ The AMICO-COSMOS galaxy cluster and group catalogue with members is available at the CDS via anonymous ftp to cdsarc.cds.unistra.fr (130.79.128.5) or via https://cdsarc.cds.unistra.fr/viz-bin/cat/J/A+A/687/A56

galaxies are largely used to detect clusters as overdensities of galaxies, by using different methods that exploit different galaxy properties. Some of the techniques widely used in literature are cluster red-sequence methods (e.g. Rykoff et al. 2014), BCG methods (e.g. Koester et al. 2007), wavelet filtering techniques (e.g. Gonzalez 2014), Voronoi tessellation methods (e.g. Ramella et al. 2001), friends-of-friends algorithms (e.g. Farrens et al. 2011), and matched filters (e.g. Postman et al. 1996; Bellagamba et al. 2011). Particularly challenging is the detection of galaxy clusters at high redshift, which requires the proper choice of techniques and galaxy properties to be used. For instance, the dominance of red passive galaxies was shown to be less robust with increasing redshift; $z \sim 1.4$ was often found as a threshold for the presence of a fraction of star-forming galaxies more consistent with that of the field as well as more irregular galaxy morphologies (e.g. Brodwin et al. 2013; Alberts et al. 2016; Strazzullo et al. 2016).

For this work we performed a cluster search with the Adaptive Matched Identifier of Clustered Objects (AMICO; Bellagamba et al. 2018; Maturi et al. 2019). This algorithm belongs to the class of linear optimal matched filters and is capable of extracting signals with maximised signal-to-noise ratio (S/N). AMICO has been chosen as one of the two algorithms for cluster detection officially adopted by the ESA Euclid mission[1] (Laureijs et al. 2011). The algorithm has distinguished itself in the context of the Euclid Cluster Finder Challenge in terms of completeness and purity when applied to mock catalogues with the expected properties of Euclid photometric catalogues (Euclid Collaboration 2019). When compared to other methods, AMICO is characterised by the possibility to search for clusters with no need for spectroscopic information and without explicit use of colour as a galaxy property. This makes it possible to search for clusters in photometric catalogues up to high redshift, and reduces the possibility to bias the selection for the presence (or absence) of cluster red-sequence. AMICO also includes an iterative detection and deblending procedure that allows the detection of smaller and blended structures by removing the imprints of sequentially detected candidate clusters. The AMICO algorithm has already been successfully applied to wide-field surveys, such as the Kilo-Degree Survey (KiDS[2]; de Jong et al. 2017), which gave origin to a cluster sample (Maturi et al. 2019) already used for several cosmological (e.g. Giocoli et al. 2021; Ingoglia et al. 2022; Lesci et al. 2022a,b; Romanello et al. 2024) and cluster galaxy population studies (e.g. Radovich et al. 2020; Puddu et al. 2021; Castignani et al. 2022, 2023).

In this work, we searched for galaxy clusters with AMICO in the COSMOS 2-deg^2 field (Scoville et al. 2007). The COSMOS survey offers the possibility to access high-quality multiwavelength data up to high redshift. COSMOS photometric galaxy catalogues have been a resource for extragalactic studies concerning galaxy properties and environment (e.g. Darvish et al. 2016; Laigle et al. 2018), including the latest release, the COSMOS2020 catalogue (Weaver et al. 2022), which has already been widely used in several works (e.g. Weaver et al. 2023; Taamoli et al. 2024; Gould et al. 2023). The availability of deep imaging and extremely accurate photometric redshifts gave us the chance to carry out this new and challenging application of AMICO. The AMICO algorithm has already been tested and applied to wide-field surveys (e.g. Maturi et al. 2019; Euclid Collaboration 2019). In this work we applied the AMICO algorithm for the first time to the new photometric data available for the COSMOS field. This cluster search with AMICO in the COSMOS field is innovative compared to past applications, for instance in terms of redshift extent, depth, and amount of area covered, and allowed the creation of a new catalogue up to $z = 2$ and down to less than $10^{13}\,M_\odot$. This was done with a twofold purpose, since it serves as a benchmark to test and improve the performances of the algorithm in a new configuration and, at the same time, it pushes the limit of cluster detection to investigate the regime of high-redshift clusters and low-mass clusters and groups.

The catalogue of galaxy clusters and groups we produced is the result of three independent runs performed by using position, photometric redshift, and magnitude in a different band for each run. The multiwavelength coverage of the COSMOS field allowed us to make a comparison with publicly available X-ray detected groups. In this work, we compared the AMICO-COSMOS catalogue with the catalogue presented in Gozaliasl et al. (2019) and exploited the availability of mass estimates to calibrate the scaling relations with AMICO mass proxies down to less than $10^{13}\,M_\odot$. We then repeated the same analysis by estimating X-ray mass with *Chandra+XMM-Newton* data at the locations of new detections as provided by AMICO and calibrated the scaling relations for a larger sample. The use of different photometric bands and the X-ray analysis allowed the comparison of the detection performances at different bands and the creation of a cluster catalogue with X-ray associated properties for each detection, including those not previously reported in X-ray public catalogues.

This paper is organised as follows. In Sect. 2 we introduce the galaxy catalogue we used as input for the cluster search. In Sect. 3 we present the fundamentals of the AMICO algorithm. In Sect. 4 we describe the application of the AMICO algorithm to this peculiar survey configuration, going through the chosen cluster model, the creation of the composite visibility mask and of the noise. In Sect. 5 we present the results of the cluster search, first by introducing the initial output of three AMICO runs, then by comparing them in order to create a final catalogue of candidates. Section 6 is dedicated to the comparison with X-ray selected clusters and the calibration of a preliminary scaling relation based on successful matches. Section 7 includes the analysis of the unmatched new detections for which we measured X-ray properties directly at the candidate locations and repeated the scaling-relation calibration with redshift dependence. In Sect. 8 we summarise the main results of this work. For the sake of simplicity, we favour the use of the term "cluster" throughout the paper to refer to both candidates with the characteristics of galaxy clusters and of galaxy groups. For this study, we assume a standard cosmology with matter density $\Omega_m = 0.3$, dark energy density $\Omega_\Lambda = 0.7$, and Hubble constant $h = 0.7$.

2. The COSMOS data sets

The Cosmic Evolution Survey (COSMOS; Scoville et al. 2007) has offered access over the years to a unique combination of deep data, with wavelength extension from radio to X-rays (e.g. Koekemoer et al. 2007; Zamojski et al. 2007; Cappelluti et al. 2009; Civano et al. 2016; Smolčić et al. 2017) and large spectroscopic coverage (e.g. Lilly et al. 2007; Hasinger et al. 2018). This has made this 2 deg^2 field a source of large galaxy samples characterised by photometric redshifts of extremely good quality up to high redshift. The field properties and accessibility have made it ideal for studying the large-scale structure and

[1] http://sci.esa.int/euclid/
[2] http://kids.strw.leidenuniv.nl/

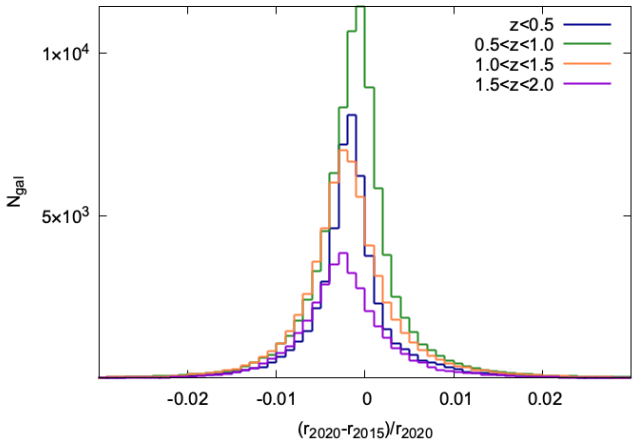

Fig. 1. Distribution of the relative magnitude scatter in the r-band for the galaxies present both in the COSMOS2020 (r_{2020}) and in the COSMOS2015 (r_{2015}) catalogues. The different colours represent different redshift bins, as labelled in the plot.

the formation and evolution of structures in the Universe (e.g. Hung et al. 2016; Cucciati et al. 2018; Laigle et al. 2018).

The photometric galaxy catalogue we used for our cluster search is the most recent release at the time of writing: the COSMOS2020 catalogue (Weaver et al. 2022). We nevertheless combined the catalogue with a sample from the previous release, COSMOS2015 (Laigle et al. 2016), due to some potential cluster galaxies missing in the COSMOS2020 selected catalogue. We visually inspected different classes of objects flagged as masked and selected a group of galaxies, labelled with `flag_peter` = 6 or 4 in the catalogue by Laigle et al. (2016), which are bright extended galaxies and galaxies close to them, potentially located in dense environments and likely belonging to clusters. These galaxies are misclassified, labelled with a general masking flag, are not identified, and have missing or unsafe photometry and/or missing redshift estimates in the newest release. Even if this galaxy sample from COSMOS2015 is statistically small, it contains typical cluster members, including several central bright galaxies that might affect the detection of some clusters and groups, especially at low and intermediate redshift.

The COSMOS2015 catalogue comprises more than half a million galaxies extracted from the $zYJHK_s$ image, with data from the Subaru (Taniguchi et al. 2015) and VISTA (McCracken et al. 2012) telescopes via `SExtractor` dual-image mode (Bertin & Arnouts 1996). Photometric redshifts, estimated using `LePhare` software (Arnouts et al. 2002; Ilbert et al. 2006), reach an accuracy better than 1% at $z < 1.2$ when compared with spectroscopic samples.

The main improvement in the COSMOS2020 catalogue with respect to the COSMOS2015 catalogue is the addition of new ultra-deep optical and NIR data from the Hyper Suprime-Cam (HSC) Subaru Strategic Program PDR2 (Aihara et al. 2019) and from UltraVISTA survey Data Release 4 (McCracken et al. 2012; Moneti et al. 2023). The use of new data is reflected in the nearly doubled number of detected sources and in the ability to reach the same photometric redshift uncertainty at nearly one magnitude deeper than in COSMOS2015. Moreover, the addition of the deep HSC-i band to the detection process increases the completeness with respect to the previous release, especially for small blue galaxies (Weaver et al. 2022).

The COSMOS2020 release includes two different catalogues produced with independent extraction methods: (1) the CLASSIC catalogue which follows the same approach used in COSMOS2015, namely it is created with `SExtractor`, after point spread function homogenisation, and (2) THE FARMER catalogue, produced by using purely parametric modelling with `The Tractor` (Lang et al. 2016; Weaver et al. 2023). Both galaxy catalogues include in turn both photometric redshifts computed using `LePhare` and `EAZY` (Brammer et al. 2008). Weaver et al. (2022) presented a detailed comparison between the different options, and showed that a very good level of consistency existed between the two redshift estimation methods and the two extraction methods.

For this work we chose to use the CLASSIC catalogue in combination with photometric redshifts estimated with `LePhare` to maximise the number of available galaxies. The CLASSIC catalogue covers a slightly larger effective area than THE FARMER, which does not return photometry in the case of model failure in the extraction process (Weaver et al. 2022). Photometric redshifts estimated using `LePhare`, also chosen for better consistency with COSMOS2015, are estimated in COSMOS2020 with a configuration similar to that used in Ilbert et al. (2013) and were found to reach per cent accuracy at the brightest i magnitudes up to a maximum value of $\sim 0.02(1+z)$ for $i < 25$, with a catastrophic failure of just a few per cent. The consistency in the source extraction and the redshift computation between COSMOS2020 and COSMOS2015 became crucial since we integrated the selected galaxy catalogue of the newest release with a sample of galaxies from COSMOS2015. In addition to choosing the option with consistent photometric redshift estimation methods, we studied the consistency of the releases in terms of magnitude. We found a slight bias increasing with redshift, which is nevertheless negligible within the analysed redshift range. For most of the galaxies present in both catalogue releases, the relative magnitude difference in the two galaxy samples is less than one per cent, as shown in Fig. 1 for the r-band. Within the studied redshift range, this magnitude difference is negligible with respect to the resolution of the cluster model, as described in Sect. 4.1.

We performed three independent runs using three different magnitudes as galaxy properties. Among the available bands, we chose to use HSC-r, UltraVISTA-Y, and UltraVISTA-H. We considered only the UltraVISTA portion of the COSMOS field, namely with RA[deg] $\in$ [149.30, 150.79] and Dec[deg] $\in$ [1.60, 2.81], where the bands used for source extraction are available as well as the bands chosen for this analysis. We searched for clusters in the unmasked fraction of this area (see Sect. 4.3), for a final effective area of 1.69 deg^2. We selected three final galaxy catalogues including all unmasked galaxies with available magnitude and photometric redshifts. We discarded galaxies with anomalies in the redshift probability distribution, $p(z)$, or with unrealistically peaked distributions that might bias the estimate of cluster properties. We performed a magnitude cut on the mode of each magnitude distribution defining the depth of the galaxy catalogues, as reported in Table 1. As a reference, the r-band galaxy catalogue we used extends to almost three magnitudes deeper than the catalogue used in the AMICO-KiDS cluster search (Maturi et al. 2019). The distribution in redshift of the selected galaxies in the three input catalogues is shown in Fig. 2 for $0 < z < 2$, where the top panel refers to the full input catalogues, while the bottom panel refers to the galaxies added from COSMOS2015 only. Table 1 summarises the properties of the input galaxy catalogues for $0 < z < 2$, with the total number of galaxies from both releases (total number of unmasked galaxies in the input catalogue) and the number of galaxies among these which are taken from the COSMOS2015 sample.

Table 1. Selected input galaxy catalogues for the three analyses with the total number of galaxies taken from both COSMOS releases ($N_{\rm gal,TOT}$) and those from COSMOS2015 ($N_{\rm gal,2015}$) in the range $0 < z < 2$.

Instrument-band	Depth	$N_{\rm gal,TOT}$	$N_{\rm gal,2015}$
HSC-r	<26.7	450 984	1854
UltraVISTA-Y	<26.1	442 449	934
UltraVISTA-H	<25.6	407 067	883

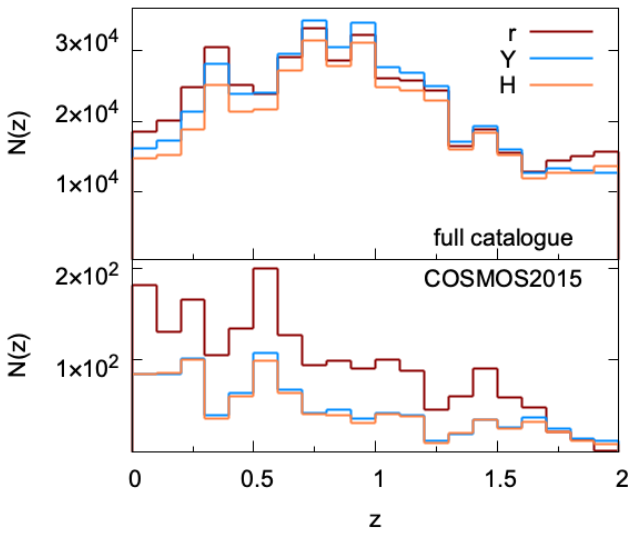

Fig. 2. Distribution of selected galaxies as a function of redshift for the three runs in r-, Y-, and H-band magnitudes in the range $0 < z < 2$. Top panel: full catalogues including selected galaxies of COSMOS2020 and the insert from COSMOS2015. Bottom panel: only galaxies belonging to the insert from COSMOS2015.

3. The algorithm for cluster detection: AMICO

AMICO (Bellagamba et al. 2018; Maturi et al. 2019) is a cluster detection algorithm based on a linear optimal matched filter (e.g. Maturi et al. 2005) that extracts a specific signal from a data set affected by a noisy background, aiming at maximising the S/N. The data are modelled as the sum of a signal component and a noise component, accounting for cluster and field galaxies, respectively. Thus, the galaxy density $D(\boldsymbol{x})$, which is a function of the galaxy properties $\boldsymbol{x}$, can be written as $D(\boldsymbol{x}) = AM_{\rm c}(\boldsymbol{x}) + N(\boldsymbol{x})$, where the signal component is expressed by an expected signal, namely the cluster model $M_{\rm c}(\boldsymbol{x})$, scaled by the so-called amplitude A, and where $N(\boldsymbol{x})$ is the noise. The amplitude is computed as a convolution of the data with a kernel defined via a constrained minimisation that guarantees an unbiased and minimum-variance estimate. The convolution filter $\Psi_{\rm c}$, in the case of noise characterised by a white power spectrum, is expressed by $\Psi_{\rm c} = \alpha^{-1}M_{\rm c}/N$, which is the ratio of the cluster model to the noise.

Each galaxy in the catalogue is characterised by a sky position $\boldsymbol{\theta}_i$; a photometric redshift probability distribution $p_i(z)$, which in this case we model with a Gaussian distribution characterised by the mode and 1σ values; and an arbitrary number of additional galaxy properties. We focus here on the simple case of one single magnitude as the galaxy property, so the set of considered properties for the ith galaxy is $\boldsymbol{x}_i = (\boldsymbol{\theta}_i, p_i(z), m_i)$, where m_i is the galaxy magnitude. Given $\boldsymbol{\theta}_{i,{\rm c}}$ the angular position of the ith galaxy with respect to the cluster centre $(\boldsymbol{\theta}_{\rm c}, z_{\rm c})$, we can write the discretised form of the amplitude as

$$A(\boldsymbol{\theta}_{\rm c}, z_{\rm c}) = \alpha^{-1}(z_{\rm c}) \sum_{i=1}^{N_{\rm gal}} \frac{M_{\rm c}(\boldsymbol{\theta}_{i,{\rm c}}, m_i) p_i(z_{\rm c})}{N(m_i, z_{\rm c})} - B(z_{\rm c}), \tag{1}$$

where α is the amplitude normalisation and B the average background contribution. The expected variance of the amplitude, given by background stochastic fluctuations and Poissonian fluctuations generated by cluster members, is expressed by

$$\sigma^2_{\rm A}(\boldsymbol{\theta}_{\rm c}, z_{\rm c}) = \alpha^{-1}(z_{\rm c}) + A(\boldsymbol{\theta}_{\rm c}, z_{\rm c}) \frac{\gamma(z_{\rm c})}{\alpha^2(z_{\rm c})}, \tag{2}$$

where γ is the cluster variance filter constant. Once we express the typical redshift probability distribution for a galaxy located at $z_{\rm c}$ as

$$q(z_{\rm c}, z) = \frac{\sum_{i=1}^{N_{\rm gal}} p_i(z - z_{\rm c} + z_{p,i}) p_i(z_{\rm c})}{\sum_{i=1}^{N_{\rm gal}} p_i(z_{\rm c})}, \tag{3}$$

being $z_{p,i}$ the mode of the redshift distribution for the ith galaxy, the above-mentioned filter constants representing amplitude normalisation, average background contribution, and cluster variance are respectively expressed by

$$\alpha(z_{\rm c}) = \int \frac{M^2_{\rm c}(\boldsymbol{\theta} - \boldsymbol{\theta}_{\rm c}, m, z_{\rm c}) q^2(z_{\rm c}, z)}{N(m, z_{\rm c})} \, {\rm d}^2\theta \, {\rm d}m \, {\rm d}z, \tag{4}$$

$$B(z_{\rm c}) = \alpha(z_{\rm c})^{-1} \int M_{\rm c}(\boldsymbol{\theta} - \boldsymbol{\theta}_{\rm c}, \boldsymbol{m}, z_{\rm c}) q(z_{\rm c}, z) \, {\rm d}^2\theta \, {\rm d}m \, {\rm d}z, \tag{5}$$

$$\gamma(z_{\rm c}) = \int \frac{M^3_{\rm c}(\boldsymbol{\theta} - \boldsymbol{\theta}_{\rm c}, \boldsymbol{m}, z_{\rm c}) q^3(z_{\rm c}, z)}{N^2(\boldsymbol{m}, z_{\rm c})} \, {\rm d}^2\theta \, {\rm d}m \, {\rm d}z. \tag{6}$$

3.1. Membership association

Using a 3D grid with resolution 0.3′ on the sky plane and 0.01 in redshift, AMICO computes the map of amplitude and selects cluster candidates by looking for peaks in the map with the highest S/N.

AMICO determines a probabilistic membership for each galaxy once the cluster position is selected. The probability of the ith galaxy belonging to the jth cluster is computed as

$$P_{i,j} = P_{F_i} \frac{A_j M_j(\boldsymbol{\theta}_i - \boldsymbol{\theta}_j, \boldsymbol{m}_i) p_i(z_j)}{A_j M_j(\boldsymbol{\theta}_i - \boldsymbol{\theta}_j, \boldsymbol{m}_i) p_i(z_j) + N(\boldsymbol{m}_i, z_j)}, \tag{7}$$

where we account for possible previous associations with other clusters through the field probability, P_{F_i}. The field probability has an initial value of 1, which decreases at each association and is exploited as a scaling factor to account for how much the galaxy is "still available" for further assignments.

The membership probability is not only used to create a catalogue of cluster members, but it is also exploited to remove the imprint of detected clusters from the amplitude map with an iterative approach. This allows the detection of blended and lower S/N candidates. The association probability is used to weight the contribution of members to the signal.

3.2. Mass proxies

The membership probability assigned by AMICO to the cluster members is also used to compute two different cluster mass proxies in addition to the natural output of the filtering process, the amplitude A. These proxies estimate the number of visible

galaxies belonging to a cluster and are referred to as apparent and intrinsic richness. The former is simply the sum of all member probabilities of the jth cluster:

$$\lambda_j = \sum_{i=1}^{N_{\rm gal}} P_{i,j}. \tag{8}$$

This proxy is related to a direct observable, but it is redshift dependent since the number of visible galaxies decreases with distance. The intrinsic richness follows the same approach, but adds constraints on magnitude and distance from the cluster centre:

$$\lambda_{\star,j} = \sum_{i=1}^{N_{\rm gal}} P_{i,j} \quad \text{with} \quad \begin{cases} m_i < m_\star(z_j) + 1.5 \\ r_i < R_{200}(z_j) \end{cases}. \tag{9}$$

Here the characteristic magnitude, $m_\star$, and the virial radius, R_{200}, are parameters fixed by the chosen cluster model (see Sect. 4.1). The intrinsic richness, $\lambda_\star$, unlike the apparent richness, has proved to be a nearly redshift independent mass proxy (Bellagamba et al. 2018; Maturi et al. 2019).

4. Applying AMICO to the COSMOS data

We applied the AMICO algorithm to the COSMOS field by running three different and independent analyses, each using one of the selected magnitudes. Even though AMICO can deal with an arbitrary number of quantities describing galaxy properties, we preferred to use one magnitude at a time, therefore without making explicit use of colour as a galaxy property. This reduces the possibility to bias the selection for the presence or absence of the cluster red-sequence. We used the following bands: HSC-r, UltraVISTA-Y, and UltraVISTA-H, down to a magnitude of 26.7, 26.1, and 25.6, respectively, as reported in Table 1. In all the analyses, each galaxy of the input catalogue is considered as a data point with ID, sky coordinates, a single magnitude, and an analytic photometric redshift probability distribution, $p(z)$, built with a Gaussian distribution characterised by $z_{\rm peak}$ and $z_{\rm min}$, $z_{\rm max}$, namely the 1σ errors.

4.1. Cluster model

The cluster model describes the signal we expect to detect, namely the expected distribution of cluster galaxies in position and magnitude as a function of redshift. This can be constructed analytically from a radial profile $\Theta(r)$, where r is the distance from the cluster centre, and from a luminosity function $\Phi(m)$:

$$M_{\rm c}(r, m) = \Theta(r)\Phi(m). \tag{10}$$

For the radial distribution we used a NFW profile (Navarro et al. 1997) with parameters from the scaling relation presented by Hennig et al. (2017), where the properties of a sample of 74 SZ-selected massive clusters detected within the overlap between the Dark Energy Survey (DES; The Dark Energy Survey Collaboration 2005) and the South Pole Telescope survey (SPT; Story et al. 2013) were studied. The sample extends up to $z \sim 1.1$. The estimate for the concentration parameter we adopted from this study is the mean full-population value $c = 3.59$ and the typical virial mass of the model was chosen to be $M_{200} = 10^{14}\, M_\odot$.

The luminosity function was assumed to follow a Schechter function (Schechter 1976):

$$\Phi(m) \propto 10^{-0.4(m-m_\star)(\alpha+1)} \exp[-10^{-0.4(m-m_\star)}]. \tag{11}$$

The faint-end slope, α, was adopted as estimated by Zenteno et al. (2016) who analysed the 26 most massive clusters of the SPT survey sample and found a mean value for the full galaxy population of $\alpha = -1.06$. The characteristic magnitude, $m_\star$, and its redshift evolution were derived by evolving a typical massive elliptical galaxy with evolutionary synthesis models via the GALEV interface (Kotulla et al. 2009). For this model we relied on a Kroupa initial mass function (Kroupa 2002) and adopted a chemically consistent approach (Kotulla et al. 2009) for a massive elliptical formed at $z = 8$ with a high-redshift, exponentially declining star formation burst. We did this following the same approach as in Castignani et al. (2022, 2023), and consistently with formation scenarios and passively evolving stellar populations in massive elliptical galaxies (e.g. Holden et al. 2004; De Lucia et al. 2006; Skelton et al. 2012; Castignani & Benoist 2016). The cluster model we built for this cluster search has a magnitude resolution of $\Delta m = 0.5$.

4.2. Noise model

The noise model, which accounts for field galaxies, can be approximated to the overall proprieties of the galaxy sample. This holds true under the assumption of negligible contribution of cluster galaxies. Although we observed overdensities localised in redshift in a noise model produced with the input galaxy catalogues, we found that the cause of these peaks is not attributed to physical overdensities (i.e. cluster galaxies), whereas it is likely due to photometric redshift accumulation points. The negligibility of cluster contribution to the noise for the COSMOS field was proven in two independent ways: (1) by removing galaxies attributed to groups with probability >50% up to $z = 1$ according to the membership catalogue produced by George et al. (2011) and (2) by taking the median of each noise pixel from non-overlapping portions of the field in order to attenuate the imprint of localised overdensities. Neither of these methods attenuated the observed peaks.

Given the small area covered by this cluster search and the small statistics of the galaxy sample with respect to past applications of AMICO to wide-field surveys, a noise regularisation was needed in order to get robust results. To regularise the noise we attributed an arbitrary large value of noise to pixels without the contribution of any galaxy. This was necessary to make the integration space finite when computing the filter constants (see Eqs. (4)–(6)), and was empirically found to successfully make the filter constants more robust.

Figure 3 shows the influence that the performed regularisation has on two filter constants in comparison with a non-regularised noise model retrieved from COSMOS data sets. The regularisation of the noise successfully smooths out the largest fluctuations of the filter constants.

4.3. Masked areas

We created a visibility mask based on the input galaxy catalogue as follows. First, we masked the pixels where saturated stars fall, using the same sample Weaver et al. (2022) used for COSMOS2020. The sample is part of the Incremental Data Release of the HSC bright-star masks by Coupon et al. (2018), extracted from the *Gaia* DR2 (Gaia Collaboration 2018), with magnitude threshold $G < 18$. We masked different areas depending on the magnitude of stars in this range by simply dividing them in two groups, brighter or fainter than the median value. Second, we masked pixels lacking HSC unmasked objects in the

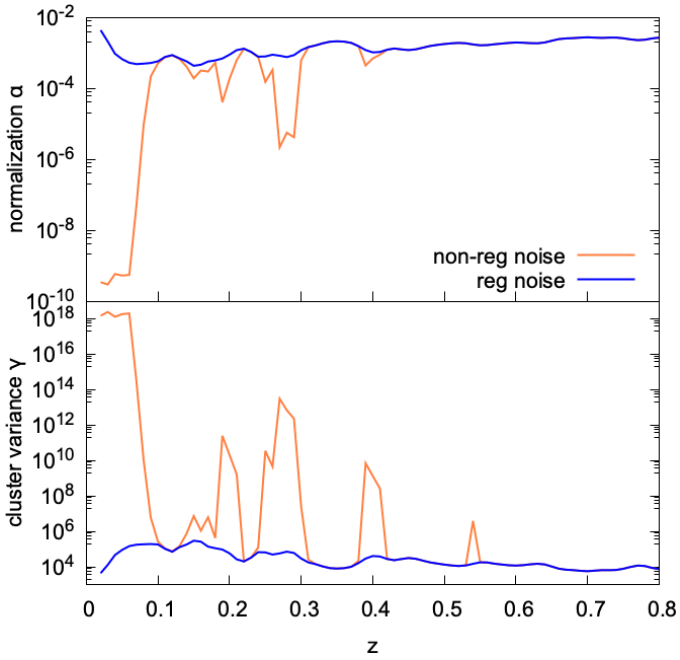

Fig. 3. Effect of noise regularisation at $z < 0.8$ on the redshift trend of two filter constants: the amplitude normalisation, α (top panel; see Eq. (4)), and the cluster variance, γ (bottom panel; see Eq. (6)). The orange line represents a typical AMICO run on COSMOS data, using the Y-band magnitude, without noise regularisation, while the blue line represents the same run with the noise assessment described in the text.

full CLASSIC catalogue in order to account for halos and diffraction spikes of bright foreground stars or other extended patterns. Finally, we masked pixels without any galaxy in the final joint COSMOS2020 and COSMOS2015 catalogue to account for the additional galaxies taken from the previous release. Masked pixels combining these criteria were used to create the final composite visibility mask. The final effective area on which the cluster search was performed is 1.69 deg^2.

5. The cluster and group catalogues

In this section we present the resulting catalogues of the cluster search performed in COSMOS with the AMICO algorithm. The candidate samples are then matched and compared and a few examples of detections are discussed.

5.1. Results of the cluster search

We performed a cluster search over the effective area of 1.69 deg^2 in the COSMOS-UltraVISTA field as previously described. We chose $(S/N)_{\rm min} = 3.0$ and cut the catalogues at $\lambda_\star > 1$, which are typical values to minimise the number of spurious or extremely poor detections in terms of galaxy content. However, as we describe in Sect. 5.2, an a posteriori cut at $S/N = 3.5$ can be adopted to select a more robust subsample of the catalogue. We produced three initial cluster catalogues from the three analyses performed by using different photometries:

r-band: We detected 893 clusters in the range $0.1 < z < 2.0$ by using the HSC-r magnitude as the galaxy property. Among these, 514 candidates (~58%) were detected with $S/N > 3.5$.

Y-band: We detected 845 clusters in the range $0.1 < z < 2.0$ by using the UltraVISTA-Y magnitude. Among these, 408 candidates (~48%) were detected with $S/N > 3.5$.

H-band: We detected 786 clusters in the range $0.1 < z < 2.0$ by using the UltraVISTA-H magnitude. Among these, 382 candidates (~49%) were detected with $S/N > 3.5$.

Figure 4 shows the distribution of the number of detections and their amplitude as a function of redshift. The minimum detectable amplitude increases as a function of redshift since the further away we observe, the harder it is to detect small clusters. Differences between the number of detected clusters and cluster properties between different runs can be due to the differences in depth and availability of galaxies in the input catalogues. This is also visible in the general trend of amplitude with redshift, which increases more steeply at $z > 1$ for the r-band catalogue with respect to the other catalogues. This is due to the larger number of available galaxies in the input catalogue.

The resulting cluster catalogues include identification number, sky coordinates, redshift, S/N, amplitude A, apparent richness λ, intrinsic richness $\lambda_\star$, likelihood, fraction of the cluster that is masked, cluster redshift probability distribution, and redshift uncertainty. In addition to the cluster catalogue, AMICO creates the list of galaxy members for each detected cluster with their membership and field probability.

5.2. Matching the r, Y, and H catalogues

We performed pairwise three-dimensional matching between the three catalogues adopting $dz = 0.05(1 + z)$ as the redshift separation and $drad = 0.5\,{\rm Mpc}\,h^{-1}$ as the physical sky separation. These values were chosen according to the uncertainties of cluster redshift and position estimates and were tested by visual inspection of preliminary matching results. In the matching procedure we used an a priori sorting of the input catalogues by amplitude, A.

We found correspondence between 561 candidate clusters detected in the r and Y analyses, which is around 63% and 66% of the two catalogues, respectively. Between the Y and H analyses 642 detections found a match, which is around 76% and 82% of the two catalogues. A total of 542 candidate clusters were matched when comparing r and H analyses, which is around 61% and 69% of the two catalogues. The results of this matching analysis are displayed in Fig. 5, where we show the redshift distribution and the S/N versus z of matched and unmatched detections for the three different pairs of catalogue combinations. As can be seen in Fig. 5 and as highlighted by the S/N distribution of matched and unmatched objects for the r versus H comparison in Fig. 6 (which is the comparison with the highest number of unmatched objects), the majority of detections without correspondence between runs have $S/N < 3.5$. This shows how this can be adopted as a reasonable and conservative S/N cut for the catalogue in order to have a more robust sample.

With two-way matching between different combinations of the three catalogues (i.e. matched whenever the detection is successfully paired in both directions of matching) and by adopting the same procedure described before, we found a total of 490 candidate clusters and groups detected independently in all the three analyses. Given the results of the matching between catalogues resulting from the three runs, we created a final catalogue containing all candidates, both matched and unmatched (counting as one the detections successfully found in more than one run according to our matching). Our final catalogue contains a total of 1269 candidate clusters and groups, given that all runs were performed with $(S/N)_{\rm min} = 3.0$. Among these, 666 candidates were detected with $S/N > 3.5$ in at least one of the runs. When referring to cluster properties of specific detections, hereafter we

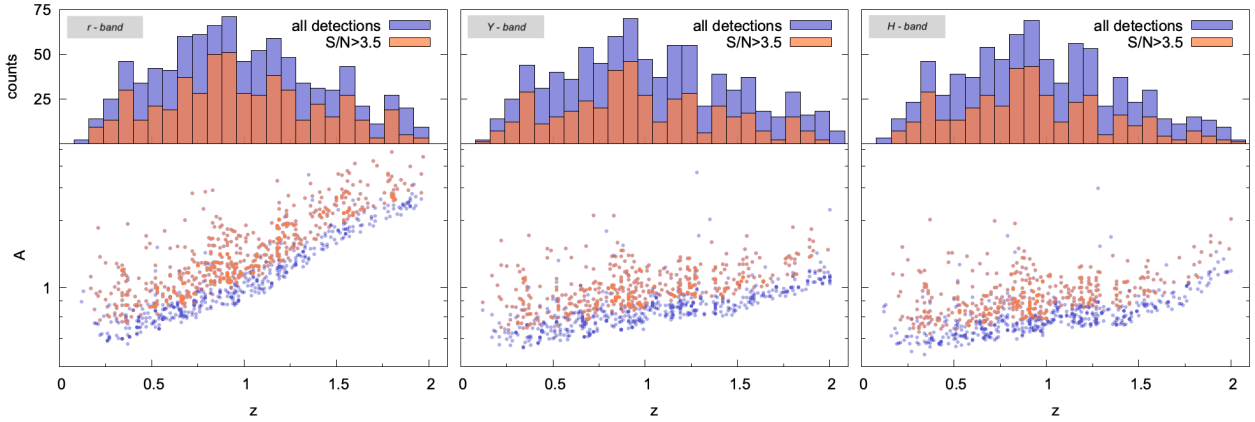

Fig. 4. Number of clusters detected (top panels) and cluster amplitude (bottom panels) as a function of redshift for the initial cluster catalogues produced by analysis in r-band (left panels), Y-band (middle panels), and H-band magnitude (right panels). The orange histograms and points highlight detections with $S/N > 3.5$.

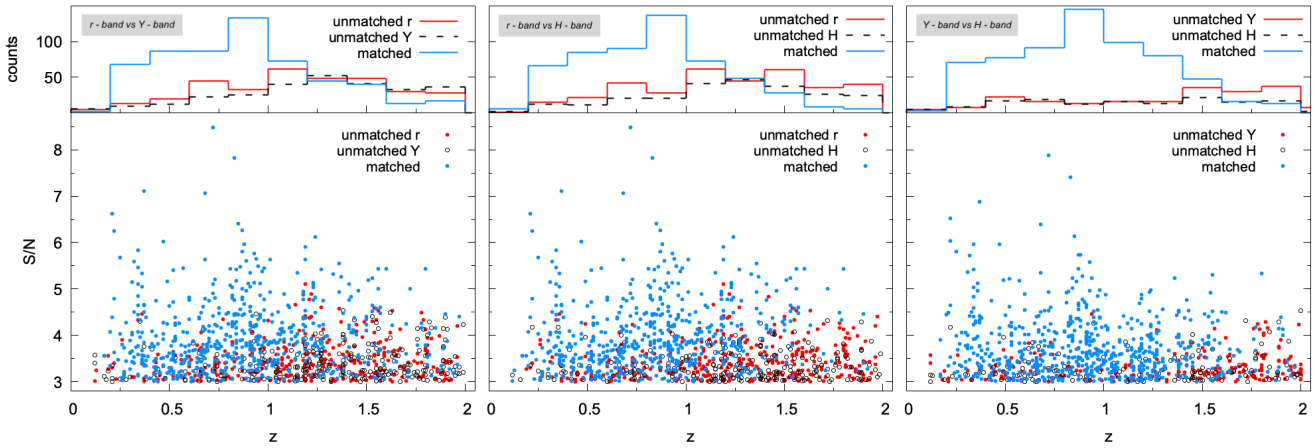

Fig. 5. Number of detected clusters (top panels) and their S/N (bottom panels) as a function of redshift for matched (blue) and unmatched (red) detections within AMICO runs: (from left to right) matching r vs. Y, r vs. H, and Y vs. H. Filled red dots and solid red lines indicate unmatched detections in the first catalogue, and empty black dots and dashed lines those in the second catalogue.

report the mean of the values obtained in the three different runs, unless otherwise specified.

5.3. Examples of detections

We visually inspected the location of a sample of detected clusters in the optical colour-composite images from HSC DR3 (Aihara et al. 2022). Figure 7 shows HSC images of four randomly chosen r-band detections, at different redshifts, with $S/N > 4.0$. Among the candidate clusters, we successfully detected the main cluster of the system identified by Smolčić et al. (2007) via a wide-angle-tail radio galaxy. Smolčić et al. (2007) found that the radio galaxy coincided with an elliptical galaxy, which was identified as the brightest cluster galaxy (BCG) of a cluster at $z \sim 0.22$. We detected this cluster in all bands and we identified 146 galaxy members (in the Y-band) with probability >50%, including the BCG (radio galaxy), which was assigned with the highest probability and has a position consistent with the centre of the cluster as found by AMICO. The structure, as detected by AMICO, is shown in Fig. 8, with associated members, amplitude, and X-ray *Chandra+XMM-Newton* (Gozaliasl et al. 2019; see Sect. 6) contours. We were not able to distinguish the assembly of more than one cluster as stated by Smolčić et al. (2007), probably because several saturated stars affected this region. Nevertheless, among the brightest galaxies associated with the cluster, we found at least three galaxies coinciding with the position of the substructures and with the peaks of the diffuse X-ray emission. This structure has been identified by AMICO as a single cluster, but the presence of these bright galaxies far from the cluster centre can indicate the grouping of several substructures.

We compared our list of candidates with other group and cluster catalogues available for the COSMOS field. Since the catalogue candidates were retrieved with different methods, and therefore present different definitions of richness and quality of the detections, it is not straightforward to make consistent comparisons and considerations. We simply include in our final catalogue the corresponding identification numbers for the 10, 182, 307, 7, 11, and 585 detections matched within $dz = 0.05(1 + z)$ and $drad = 0.5\,\mathrm{Mpc}\,h^{-1}$, from the catalogues by Zatloukal et al. (2007), Knobel et al. (2009, 2012), Castignani et al. (2014), Iovino et al. (2016), and Sarron & Conselice (2021), respectively.

One of the goals of this study was to search for high-redshift clusters. We detected 273 clusters at $z > 1.5$, of which 125 were detected with $S/N > 3.5$ in at least one run. We

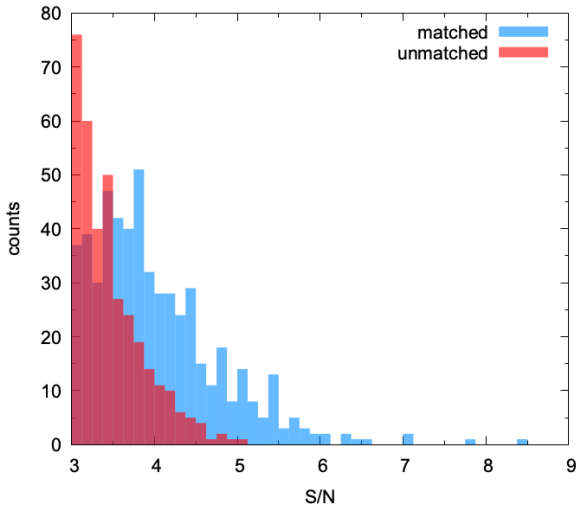

Fig. 6. Distribution of matched (blue) and unmatched (red) cluster detections in the comparison r vs. H, as a function of signal-to-noise ratio. Most of the unmatched detections have $S/N < 3.5$.

found that 111 common identifications with the catalogue by Sarron & Conselice (2021) have $z > 1.5$, of which 3 were also detected by Zatloukal et al. (2007).

Clusters overlapping along the line of sight. We performed two-dimensional matching on our final catalogue (without using redshift information), and we found 269 sets[3] of detections lying within 0.02 deg from each other. Some of these cases are in a configuration that makes it challenging to detect them, and therefore the background objects are often not known in the literature. For instance, we found that 116 sets of detections (of which 96 are pairs) have a sky separation ≤0.01 deg, involving a total of 253 objects that are almost in perfect alignment with one or more objects along the line of sight. An example of this kind of detection pair is shown in Fig. 9, where an already-known cluster at $z = 0.47$ (e.g. Gozaliasl et al. 2019; Knobel et al. 2012; Sarron & Conselice 2021) is virtually aligned with a background cluster at $z = 1.56$, which is not included, for instance, in most optical and X-ray cluster catalogues. The identification of these sets of detections is important in this cluster search, where the number of detected objects per square degree is high. In particular, having several detections close to each other on the sky plane can bias the estimation of X-ray properties. This is why we used the information about the position of these sets of detections to clean the catalogue for the calibration of the scaling relation described in Sect. 6.

5.4. Spectroscopic counterparts

We assigned spectroscopic counterparts to cluster members associated by AMICO by making use of a sample of galaxies from 13 public spectroscopic surveys (zCOSMOS-b, Lilly et al. 2007; PRIMUS, Coil et al. 2011; Cool et al. 2013; GEEC2, Balogh et al. 2014; FORS2, Comparat et al. 2015; DEIMOS, Hasinger et al. 2018; VIS3COS, Paulino-Afonso et al. 2018; hCOSMOS, Damjanov et al. 2018; FMOS-COSMOS, Kashino et al. 2019; C3R2, Masters et al. 2019; MUSE, Rosani et al. 2020; LEGA-C, van der Wel et al. 2021; MAGIC, Epinat 2021; Abril-Melgarejo et al. 2021; Epinat et al. 2024; DESI, DESI Collaboration 2023) collected in the COSMOS Spectroscopic Redshift Compilation (Khostovan et al., in prep.). We found that 612, 741, and 720 cluster detections have at least one member with spectroscopic redshift associated with the cluster with a probability >50%, in the r-, Y-, and H-band analyses, respectively. Among these, 373, 449, and 454 (i.e. 61%, 61%, and 63%) have more than three members with a spectroscopic redshift. All of these cluster candidates have a cluster redshift assigned by AMICO compatible with $z_{\rm spec}$, which is defined as the mean spectroscopic redshift of the associated members, being $\Delta z/(1 + z_{\rm spec}) < 0.03$. If we consider the final catalogue obtained by matching detections between the three different runs (as described in Sect. 5.2), the total effective number of detections with mean spectroscopic redshift based on more than three member galaxies is 567. All of these detections have a mean spectroscopic redshift compatible with that assigned by AMICO.

6. Comparison with X-ray group catalogues

We performed a comparative analysis of the AMICO detections with the X-ray selected groups presented in the work by Gozaliasl et al. (2019). In this work a catalogue of galaxy groups was produced for the COSMOS field by using *Chandra* (Elvis et al. 2009; Civano et al. 2016) and *XMM-Newton* (Hasinger et al. 2007; Cappelluti et al. 2009) 0.5–2.0 keV combined data, cleaned via wavelet transform (Vikhlinin et al. 1998).

The catalogue contains 247 groups covering the range $0.08 \leq z < 1.53$ and with masses of $M_{200} = 8\times10^{12}$–$3\times10^{14}\,M_{\odot}$. Virial masses were estimated via the scaling relation derived through stacked weak lensing analysis by Leauthaud et al. (2010). This X-ray selected catalogue is a revised and extended version of the COSMOS group catalogues presented in Finoguenov et al. (2007) and George et al. (2011). To optically validate the X-ray extended sources and estimate their redshifts, both spectroscopic (Hasinger et al. 2018) and photometric (Ilbert et al. 2009; Laigle et al. 2016; McCracken et al. 2012) galaxy samples were used. Data reduction and member identification, performed via a refined red-sequence approach, are described in detail in George et al. (2011) and Gozaliasl et al. (2019).

We performed three-dimensional matching within $dz = 0.05(1 + z)$ and $drad = 0.5\,{\rm Mpc}\,h^{-1}$. We found 104 successful matches for the r-band run, 107 matches for the Y-band run, and 99 matches for the H-band run. If we consider AMICO detections matched within different runs, the total number of detections with correspondence in the X-ray catalogue by Gozaliasl et al. (2019) is 122, or 55% of the X-ray detections. For this comparison, we considered consistent volumes occupied by the cluster searches, namely accounting for different redshift extent and effective unmasked areas covered. This comparison displayed a general good matching quality with most of the successfully paired detections lying within $0.1\,{\rm Mpc}\,h^{-1}$ and within a redshift scatter of 0.02. We found a slight and negligible redshift bias: redshift estimates for AMICO are slightly smaller with respect to X-ray identifications, with an average bias of $\Delta z/(1 + z) \approx -0.002 \pm 0.001$.

6.1. Quality flags

Gozaliasl et al. (2019) included four quality flags in their cluster catalogue. Flag 1 labels the safest detections, with spectroscopic members; flag 2 is for cases of foreground or background contamination; flag 3 signals a lack of spectroscopic counterparts; and flag 4 is assigned to the least safe sample, with ambiguous optical counterpart association. In our comparative analysis, we

[3] Pairs or groups of more than two detections.

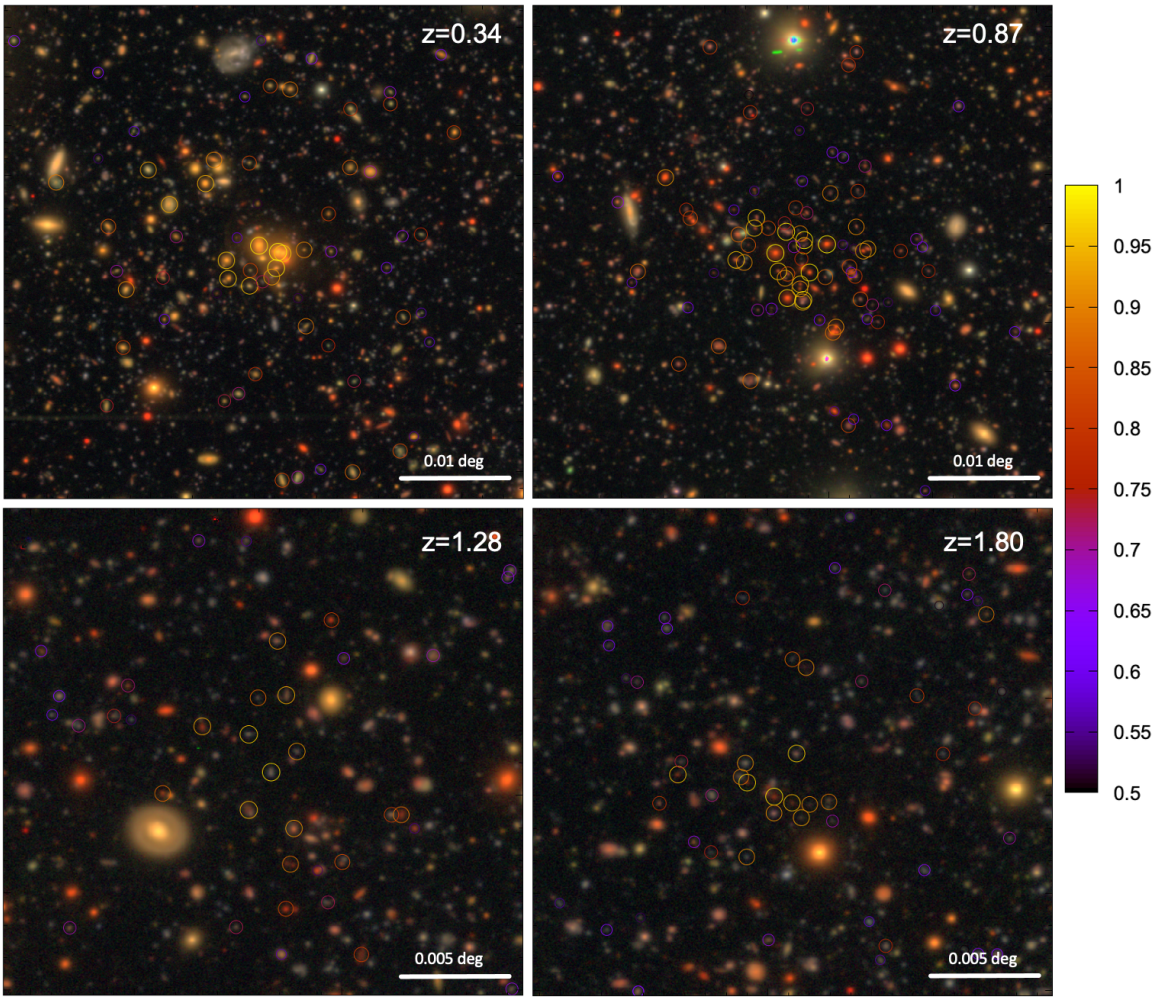

Fig. 7. Four examples of detections at different redshifts as identified in the *r*-band run. Stamps are HSC *g*, *r*, *i* colour-composite images centred on the AMICO detection, with a side of 0.05 deg for the top panels and 0.025 deg for the bottom panels. The circles indicate the associated galaxies, sized and coloured according to their association probability (see colour bar at right). Top left: candidate at $z = 0.34$ with $\lambda_\star \sim 17$; top right: candidate at $z = 0.87$ with $\lambda_\star \sim 27$; bottom left: candidate at $z = 1.28$ with $\lambda_\star \sim 26$; bottom right: candidate at $z = 1.80$ with $\lambda_\star \sim 40$.

found that 77% of the successful matches with AMICO catalogues are part of the safest X-ray sample. The safest sample of X-ray detections has more successful matches than unsuccessful matches, while for the clusters flagged with 2, 3, and 4 the opposite is true: around 57% of the problematic detections in the X-rays (flag 2, 3, or 4) do not pair with any AMICO detection. This can be read as an indication of the reliability of the flagging system by Gozaliasl et al. (2019), and therefore the general reliability of the safest X-ray candidate clusters (flag 1).

6.2. The r, Y, and H analyses when compared with X-rays

A total of 86 clusters have been found in all three AMICO catalogues and successfully matched with the catalogue by Gozaliasl et al. (2019). We can take the X-ray catalogue as a reference to make considerations on the different runs. We need to take into account only the common volume, so we restrict this comparison to the redshift range covered by the X-ray catalogue. The catalogue produced by the *Y*-band run and *r*-band run appears to be more complete with respect to the X-ray reference, having 107 and 104 matched clusters, respectively. Then, we can consider the relative number of matches for those detections that are found by AMICO in only one of the runs, which we refer to as "unique". Nevertheless, we found that the *r*-run matches only ∼4% of its unique detections, whereas ∼7% of unique *Y* and *H* detections are paired with X-ray sources.

6.3. Mass-observable scaling relations

We studied the relation between mass proxies provided by AMICO and X-ray derived mass for the sample of successfully matched clusters. The X-ray catalogue by Gozaliasl et al. (2019) comprises the 0.1−2.4 keV rest frame X-ray luminosity (L_X) measured within R_{500} and the virial mass M_{200} estimated through the scaling relation presented by Leauthaud et al. (2010). We studied the relation between X-ray virial mass (and luminosity) with AMICO amplitude (A) and with intrinsic richness ($\lambda_\star$). For this analysis we used only detections flagged as safe and with spectroscopic counterparts (flag 1 in Gozaliasl et al. 2019) that do not fall within 0.02 deg of another detection with $\lambda_\star > 20$ and identified with $S/N > 3.5$. This reduces the possibility of introducing outliers due to projection effects and contamination of a nearby object.

Mass-observable calibration from AMICO mass-proxies was performed for the AMICO-KiDS cluster sample (Maturi et al. 2019) via stacked weak-lensing analysis by Bellagamba et al.

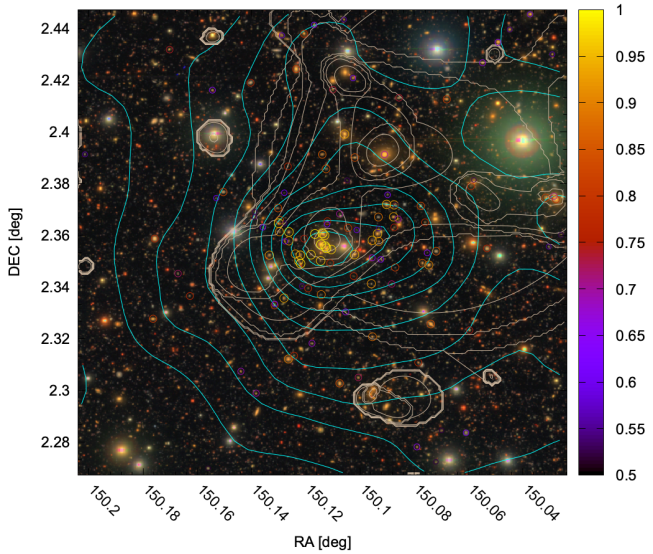

Fig. 8. Cluster substructures at $z = 0.22$ found by Smolčić et al. (2007) via a radio-BCG, as detected by AMICO. The circles indicate assigned members with colour-coded probability (see colour bar at right) and are overlaid with AMICO amplitude and X-ray contours (cyan and white, respectively).

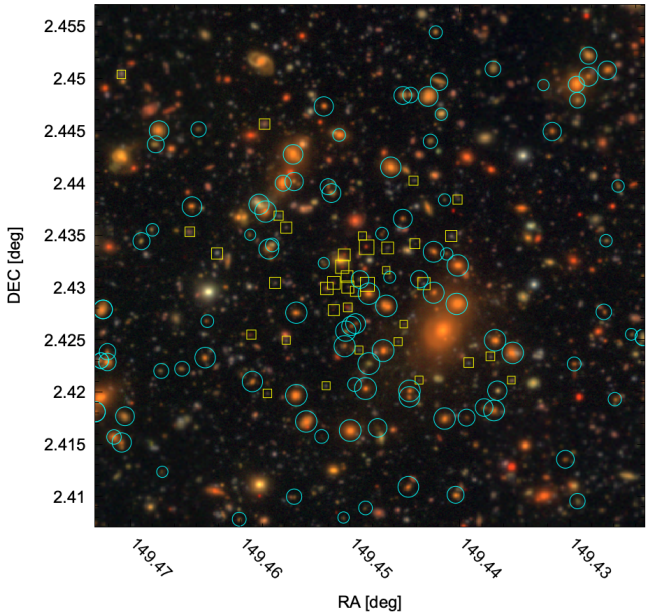

Fig. 9. Pair of detections aligned along the line of sight, as detected in the Y-band run. Members of the foreground cluster, located at $z = 0.47$, are indicated by cyan circles. The yellow squares indicate background cluster galaxies ($z = 1.56$). The size of the circles and squares is proportional to the membership probability. The HSC g, r, i composite image has a size of 0.05 deg and is centred on the background cluster.

(2019). We used the scaling relation expression used by Bellagamba et al. (2019) to fit the data for the matched cluster sample

$$\log \frac{M_{200}}{10^{14}\,M_\odot} = \alpha + \beta \log \frac{O}{O_{\rm piv}} + \gamma \log \frac{E(z)}{E(z_{\rm ref})}, \quad (12)$$

with O being the AMICO mass proxy (i.e. A or $\lambda_\star$) and $O_{\rm piv}$ its median value in the considered sample. In this part of the analysis we neglected the redshift dependency term of the relation ($\gamma = 0$) since the limited size of our sample does not allow robust analyses of redshift evolution. The fitting analyses were performed by taking into account the 1σ errors for X-ray mass, the amplitude variance (Eq. (2)), and the square root of $\lambda_\star$. We made use of the R package for LInear Regression in Astronomy (`LIRA`) described in Sereno (2016). The best-fit parameters are reported in Table 2 and the corresponding relations shown in Fig. 10. A defined relation is visible in almost all combinations among the catalogues, with a generally smaller scatter for the results of the r-band run with respect to the analyses using other photometries. The large scatter is expected for a sample extending over this wide range of masses. Detections indicated with squares in Fig. 10 are the detections used for the scaling relation fit (i.e. belonging to the safest sample detected in the X-rays) with reduced chances to have foreground or background contamination, and they all have spectroscopic members. The studied sample extends down to low masses, with the least massive matched cluster having $M_{200} \approx 9.3 \times 10^{12}\,M_\odot$ and $L_X \approx 3.3 \times 10^{41}$ erg s^{-1}.

Table 2. Mass-proxy scaling relation parameters and pivot values (see Eq. (12)) based on detections matched with the group catalogue by Gozaliasl et al. (2019).

	α	β	$O_{\rm piv}$
r-band			
$\lambda_\star$	-0.320 ± 0.025	0.780 ± 0.129	21
A	-0.311 ± 0.025	0.917 ± 0.151	1.4
Y-band			
$\lambda_\star$	-0.351 ± 0.026	0.961 ± 0.146	15
A	-0.330 ± 0.026	1.155 ± 0.198	1.0
H-band			
$\lambda_\star$	-0.352 ± 0.027	1.027 ± 0.145	15
A	-0.341 ± 0.027	1.132 ± 0.180	0.9

7. X-ray counterparts for new detections

After matching AMICO detections and X-ray selected groups by Gozaliasl et al. (2019), we studied the sample of non-matched detections and looked for their possible X-ray counterparts. We measured X-ray properties for these detections directly at their locations as identified by AMICO.

We used the combined *Chandra* and *XMM-Newton* maps of emission residuals in the 0.5−2 keV band after removing instrumental and sky background as well as unresolved X-ray emission. *XMM-Newton* provides approximately 70% of the sensitivity in the combined data. To test the effect of the total flux including the unresolved emission, we only used the *XMM-Newton* data; compared to *Chandra*, these data have a larger reduction in sensitivity due the removal of the contamination from nearby point-sources. In most cases, however, there is no contamination and an upper limit using the *XMM-Newton* data without point-source cleaning is the most constraining. The data reduction in producing the maps is identical to the analysis published by Gozaliasl et al. (2019). Using the redshifts of the AMICO clusters, we estimated the count rates inside the 200 kpc radius, and in obtaining the X-ray properties we extrapolated these numbers to the iteratively estimated R_{500} radius, following the procedure outlined in Finoguenov et al. (2007). The size of the aperture closely matches the expected size of the emission zones of the AMICO clusters found below the limit of the published X-ray catalogues in COSMOS, and so the flux extrapolations are

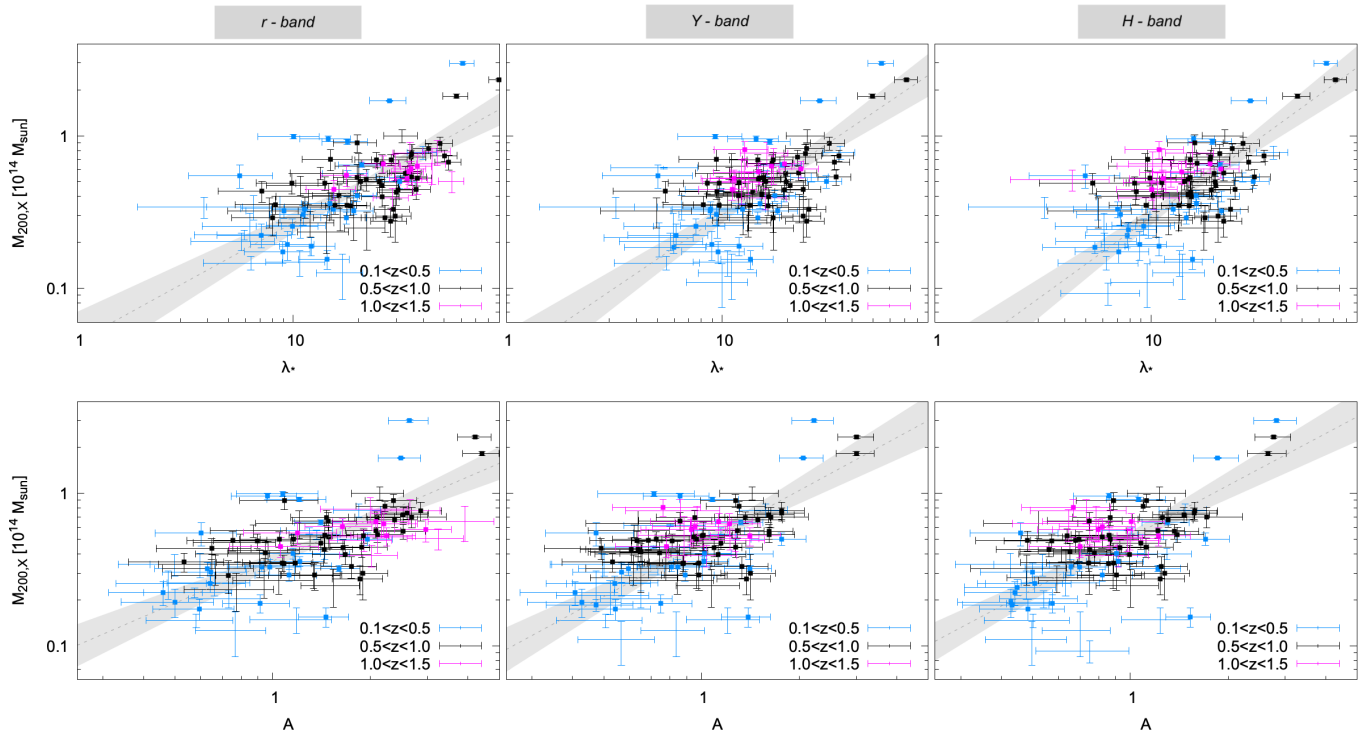

Fig. 10. Relation between X-ray mass and richness (top panels) or amplitude (bottom panels) for the X-ray matched clusters in the catalogue by Gozaliasl et al. (2019) in the range $z \in [0.1, 1.5]$. From left to right: detections retrieved from analysis in r-, Y-, and H-band. The different colours refer to different redshift bins (see legend). The grey dashed line and shaded area indicate the best-fitting relation with the corresponding 1σ errors. Data points marked by squares are the detections belonging to the safest sample in the X-ray catalogue and without foreground, background, or nearby contamination. Error bar points without a central square are matched detections not used for the scaling relation calibration.

minimal, while the overlap in the extraction zones between neighbouring clusters is not significant at $z > 0.2$.

We kept only detections with significant X-ray emission by cutting at flux significance above the 1σ limit. The total number of new detections with X-ray flux estimates above the significance limit is 500 out of the 1147 analysed candidates (~44%). If we consider only objects detected by AMICO with $S/N > 3.5$, there are 267 with significant X-ray emission out of the total 577 analysed candidates (~46%).

By adding together successful matches with the X-ray group catalogue and AMICO candidates with significant X-ray flux estimates, we created a sample of 622 candidate groups and clusters with optical and X-ray properties up to $z = 2$ and down to less than $10^{13}\,M_{\odot}$.

We repeated the calibration of the relation between AMICO mass proxies and X-ray mass, this time for the full sample of AMICO detections with X-ray estimates. In order not to include biased estimates due to foreground, background, or nearby contamination, we rejected all detections lying within 0.02 deg of the centre of another rich detection or lying on the extended X-ray emission of a bright cluster. This left us with 222 detections, which we used to calibrate the scaling relations. In Fig. 11 we show the distribution in redshift of the new detections analysed for the Y-band run catalogue, displaying the detections with and without (blue and grey) significant X-ray flux and the ones eventually selected for the study of the mass-observable scaling relations (black solid line). In Fig. 12, we show the consistency between detections matched with the X-ray catalogue (grey error bars) and new detections with X-ray estimates above the significance limit (coloured points), used for the scaling-relation calibration. Most of the new detections lie within the scatter of the catalogue-matched detections, consistently with the trends found

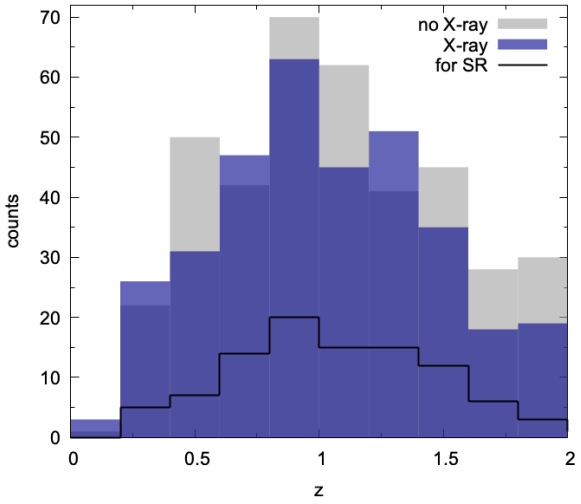

Fig. 11. Distribution of the redshifts of new detections analysed in X-rays (from the Y-band run catalogue). The grey histogram represents detections having X-ray flux below the 1σ significance limit. The blue histogram refers to detections with significant X-ray emission ($\sigma > 1$). The solid line highlights the subsample selected to study the scaling relation (SR) between AMICO mass-proxies and X-ray mass.

by the best-fitting scaling relations. We found that at fixed amplitude or $\lambda_{\star}$, new detections tend to be on average less luminous or less massive when compared to successful matches with the X-ray catalogue. This is due to the lower X-ray S/N level adopted in our analysis here, and it shows the high

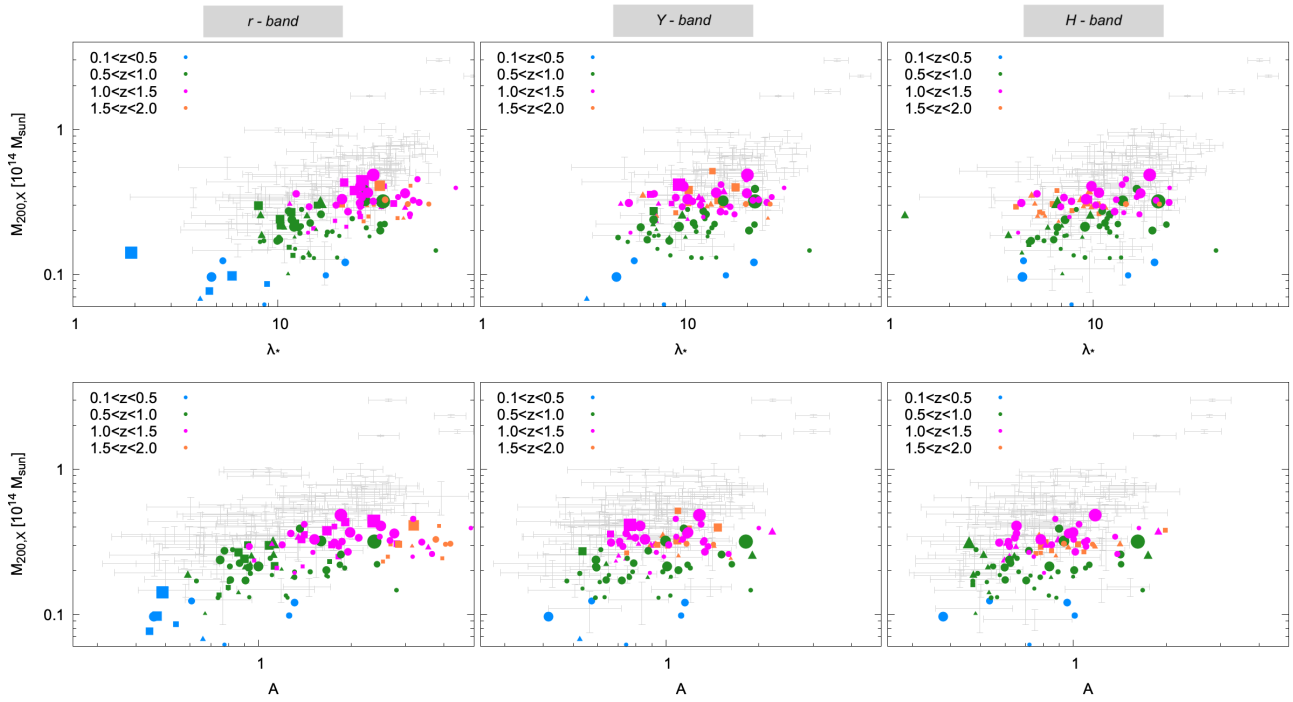

Fig. 12. Same as in Fig. 10, but for the sample of new detections with X-ray flux estimates selected for the scaling relation study (coloured points) in the full redshift range, $z \in [0.1, 2.0]$. From left to right: detections from analysis in the *r*-, *Y*-, and *H*-band. The different colours refer to the different redshift bins, as labelled in each panel. Circles are detections found in all three runs, triangles are found in two out of three runs, and squares indicate the unique detections from respective runs. The size of the symbols is proportional to the X-ray flux significance. As a reference, the grey error bars in the background indicate the detections used for the scaling relation derived from the direct matches with the X-ray catalogue (the same displayed in Fig. 10).

completeness in the identification of bright X-ray extended sources in the Gozaliasl et al. (2019) catalogue.

7.1. Redshift dependence of the scaling relations

If we consider the whole sample of detections, including successful matches with the X-ray catalogue and the new detections with X-ray flux estimates, we have the opportunity to study the scaling relations for clusters and groups extending up to $z \sim 2$ and over a wide range of mass and richness. This also allows a study of the redshift-dependence of the scaling relations. We considered the scaling relation in Eq. (12), this time including the z-dependent term (i.e. $\gamma \neq 0$).

We chose $z_{\rm ref} = 0.9$, namely the median redshift of the entire studied sample. The results of the fitting analysis including the redshift dependence term, the scatter standard deviation and the chosen pivot values, are shown in Table 3. The best-fitting relations are also shown in Fig. 13 where the data points are divided into four redshift bins with the relevant scaling relations computed at the typical redshifts of the bins ($z = [0.4, 0.8, 1.2, 1.6]$).

We found a negative redshift dependence for the *r*-band detected clusters and groups, for which at fixed amplitude or $\lambda_\star$ more distant objects tend to have lower masses. This trend seems to fade out for redder bands, although there is a negligible hint of an inverted trend for the relation $M_{200} - \lambda_\star$ in the *H*-band catalogue.

7.2. New detections without X-ray counterparts

As mentioned above, nearly half of the detections analysed in the X-rays were found not to have flux significance above unity. The relative number of new detections with and without significant X-ray flux does not seem to be significantly affected by cuts in S/N or redshift (e.g. ∼43% of analysed new detections still have $\sigma > 1$ and $S/N > 4.0$ at $z < 1$). Among these detections we found and visually inspected several examples of clusters with a significant number of assigned galaxy members. In particular, we selected 116 groups with $\lambda_\star > 20$ (i.e. among our richest detections), detected with $S/N > 4.0$ at $z < 1.6$, that were found to have X-ray flux significance below 2σ. We chose this threshold in order to include both detections below the significance limit and with low significance ($1 < \sigma < 2$). We found a few cases of correspondence or vicinity to X-ray point sources. Thus, we investigated the impact of point-source removal in estimating the flux and luminosity of extended sources. We did so, by repeating the measurements of X-ray properties for these 116 detections by considering the X-ray image without removing the point-sources. Undoubtedly, this represents a significant improvement for most of the analysed sources, as seen in Fig. 14, where we show the relation between $L_{\rm X}$ and $\lambda_\star$ for this sample (compared to the scaling relation found for the full sample and the 2σ scatter) with (top panel) and without (bottom panel) point-source removal. Most of the selected detections become consistent with the rest of the sample by reintroducing the removed flux. Nevertheless, this does not seem to be the case for two of the detections. These two outliers do not display a significant improvement in their position with respect to the rest of the sample, even with increased flux significance. One of the two outliers, the object with the lowest richness, was found in all three runs at $z = 0.36$, with $S/N \sim 5$, $\lambda_\star \sim 19$, $A \sim 1$, but with very low X-ray luminosity and large errors. The second object was instead found at $z = 0.68$, and for simplicity we refer to it as detection 5.

Table 3. Mass-proxy scaling relation parameters and pivot values (see Eq. (12)) including redshift dependence based on the full selected sample with X-ray flux estimate.

	α	β	γ	σ	$O_{\rm piv}$	$z_{\rm ref}$
r-band						
$\lambda_\star$	-0.498 ± 0.019	0.954 ± 0.105	-0.966 ± 0.241	0.170 ± 0.016	20	0.9
A	-0.516 ± 0.021	1.098 ± 0.151	-1.309 ± 0.319	0.182 ± 0.017	1.4	
Y-band						
$\lambda_\star$	-0.482 ± 0.019	0.931 ± 0.110	-0.010 ± 0.172	0.160 ± 0.016	13	0.9
A	-0.452 ± 0.020	1.232 ± 0.187	-0.206 ± 0.194	0.171 ± 0.018	1.0	
H-band						
$\lambda_\star$	-0.516 ± 0.020	0.962 ± 0.103	0.424 ± 0.182	0.145 ± 0.017	11	0.9
A	-0.519 ± 0.022	1.220 ± 0.170	-0.094 ± 0.194	0.166 ± 0.018	0.8	

Notes. The standard deviation of the scatter σ is given in $\log_{10}$ space, being the scaling relations in the form $Y = \alpha + \beta X + \gamma Z \pm \sigma$, with $Y = \alpha + \beta X + \gamma Z$ referring to Eq. (12).

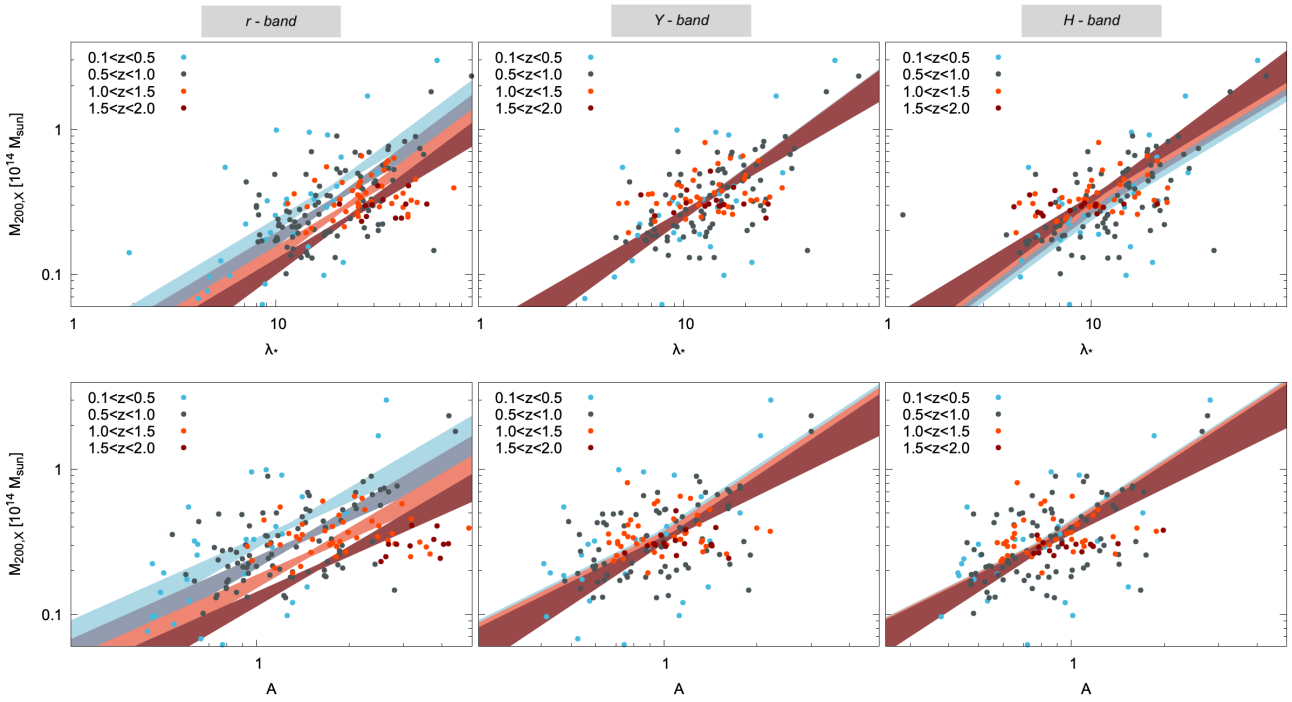

Fig. 13. Relation between X-ray mass and richness (top panels) or amplitude (bottom panels) for the full sample including matched detections with the X-ray catalogue and new detections with X-ray flux estimate in the full redshift range, $z \in [0.1, 2.0]$. From left to right: detections from analysis in *r*-, *Y*-, and *H*-band. The different colours refer to the different redshift bins, as labelled in the plot. The redshift-dependent best-fitting relation is shown for typical redshift values representing the four redshift bins, $z = [0.4, 0.8, 1.2, 1.6]$ (z increases from light blue to dark red) and with their 1σ error region. The best-fit parameters are also reported in Table 3. The redshift trend visible for *r*-band-based detections fades out for redder bands, where the scaling relations become consistent with no redshift dependence.

Detection 5 is one of the richest detections without X-ray flux significance above 2.0 and it has been detected with high signal-to-noise ratio in all AMICO runs ($S/N = 6.6$). Its intrinsic richness, for instance, in the *r*-band analysis is $\lambda_\star \sim 59$. It was found at $z = 0.68$, with ∼200 galaxy members assigned with probability larger than 50% (among these, almost half are assigned with probability >75%). This is an example of a detection whose X-ray properties measured without point-source removal did not improve sufficiently for it to become consistent with the rest of the sample in terms of the relation between optical and X-ray properties. Detection 5 is shown in Fig. 15, indicated by an arrow, with X-ray luminosity measured with and without point-source removal. The cluster redshift probability distribution, $P_{\rm cl}(z)$, of detection 5 shows no anomalies and it is consistent with the $P_{\rm cl}(z)$ of clusters at similar redshift and with similar richness, which have also been found via X-ray selection.

This interesting detection is compatible with being part of the COSMOS wall (Iovino et al. 2016). Using the same data used by Abril-Melgarejo et al. (2021), retrieved with MUSE (Epinat 2021; Epinat et al. 2024; Bacon et al. 2010), we performed our dynamical analysis. The two groups mentioned in Abril-Melgarejo et al. (2021, CG84 and CG84b) are responsible for the two peaks in the redshift distribution of AMICO members, when considering spectroscopic redshifts, centred at $z = 0.6808$ (group 1) and $z = 0.6963$ (group 2). Running the `Clean` algorithm (Mamon et al. 2013) on these two peaks and considering $\pm 2000\,{\rm km\,s^{-1}}$ around each peak, results in the following characteristics for the two groups: group 1 has 19 clean

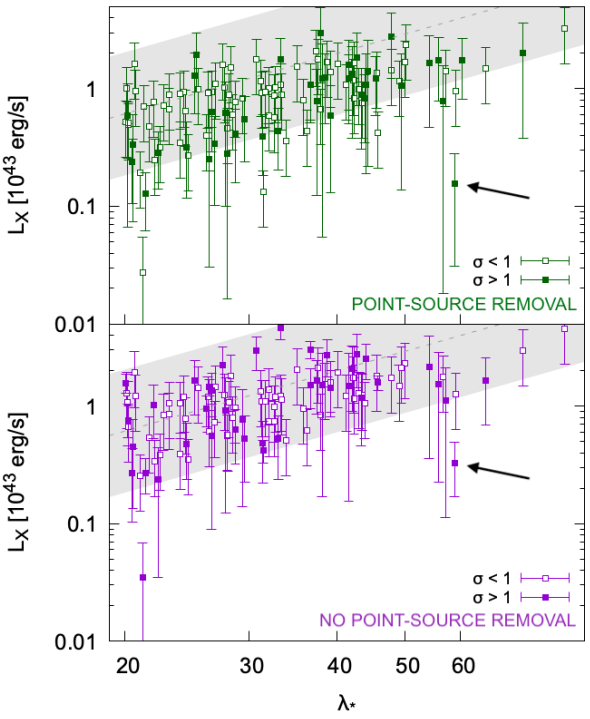

Fig. 14. Relation between X-ray luminosity and intrinsic richness for the sample of richest detections ($\lambda_\star > 20$, $S/N > 4.0$, $z < 1.6$) that were found to have non-significant X-ray emission, with X-ray measurements performed with (top panel) and without (bottom panel) point-source removal. Empty squares are detections with X-ray flux below the 1σ significance limit. The grey shaded area in the background is the 2σ scatter region relative to the L_X–$\lambda_\star$ relation found at z_{ref} for the full r-band-detected sample.

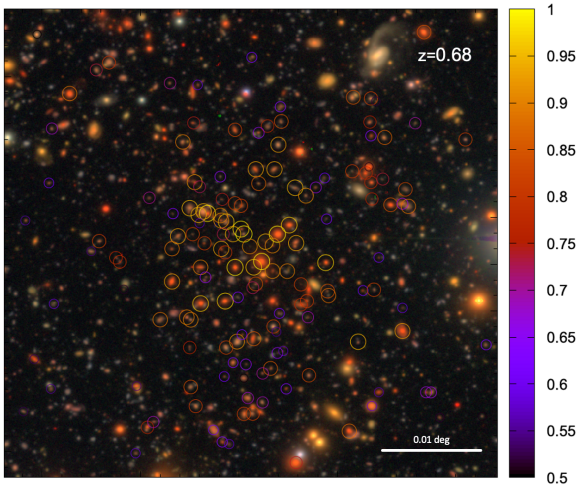

Fig. 15. Detection 5: candidate cluster detected at $z = 0.68$ with around 200 member galaxies ($\lambda_\star \sim 59$ in the r-band), without significant X-ray emission, even without point-source removal.

spectroscopic members, velocity dispersion of $263 \pm 54\,\mathrm{km\,s^{-1}}$, and a corresponding radius, $R_{200} = 397\,\mathrm{kpc}$; group 2 has 7 spectroscopic members, velocity dispersion of $170 \pm 62\,\mathrm{km\,s^{-1}}$, and $R_{200} = 254\,\mathrm{kpc}$. We note that the mass estimates reported in Abril-Melgarejo et al. (2021) are associated with measuring higher values of velocity dispersion (of around $370\,\mathrm{km\,s^{-1}}$) compared to our estimate, which we attribute to the contamination of interlopers, which in our analysis are more efficiently rejected. The number of member galaxies reported in Abril-Melgarejo et al. (2021) is indeed much higher: 35 and 31 (compared to our 19 and 7). The presence of interlopers, possibly arranged in a filamentary structure elongated along the line of sight, is reflected in the high richness measured by AMICO, given by the presence of a large number of galaxies within the redshift range accessible to the photometric redshifts, and in the relatively small X-ray flux produced by this structure, which is compatible with our spectroscopic mass estimate.

8. Conclusions

We robustly detected galaxy clusters and groups in the range $0.1 < z < 2$ by applying the AMICO algorithm to a photometric galaxy sample mostly based on the COSMOS2020 catalogue. We did this in three independent runs by using magnitudes in three different bands as galaxy properties: r-, Y-, and H-band. The final catalogue contains 1269 candidate clusters and groups among which 666 were detected with $S/N > 3.5$ in at least one of the runs. Among the detected clusters, 490 were detected in all three runs. All three runs provided us with new detections.

The main achievements of this study can be summarised as follows:

1. With the creation of a suitable cluster model, a composite mask, and the proper regularisation of the noise model, we found that the AMICO algorithm is efficient in detecting clusters, even in peculiar survey configurations such as the deep 2-deg^2 COSMOS field.
2. We found 122 correspondences with the most recent X-ray selected group catalogue for the COSMOS field. Additionally, we confirmed X-ray emission with flux significance larger than 1.0 for another 500 AMICO detections, for a total sample of 622 AMICO candidate clusters and groups with associated X-ray properties up to $z = 2$.
3. The comparison with the X-rays allowed the calibration of the scaling relations between AMICO mass-proxies and X-ray mass up to $z = 2$ and down to less than $10^{13}\,M_\odot$. We found that the new detections with X-ray emission are consistent with the rest of the sample in terms of the relation between X-ray and optical properties.
4. The inclusion of the redshift dependence term in the scaling relation analysis showed that the Y-band and the H-band magnitudes used as galaxy properties for the cluster search result in a more stable relation between X-ray mass and AMICO richness and amplitude (with respect to the r-band magnitude), which is an important result for setting the redshift dependence of the calibration.
5. We investigated the impact of point-source removal on X-ray estimates and found that in many cases this can underestimate X-ray luminosity. Nevertheless, we found an interesting example of an underluminous X-ray object with respect to its galaxy content as detected by AMICO. This is possibly due to the presence of interloper galaxies arranged in a filamentary structure along the line of sight.

The creation of such a cluster catalogue for the deep COSMOS field, including robust mass proxies and lists of cluster members, paves the way for different kinds of studies. This cluster catalogue is a resource for the study of cluster galaxy population and galaxy evolution and for the study of the formation, evolution, and physics of clusters themselves. Moreover, this work represents a key step towards the successful exploitation of the AMICO algorithm in other peculiar survey configurations, and proves the importance of selecting suitable input parameters.

Acknowledgements. We gratefully acknowledge the contribution of the entire COSMOS collaboration, consisting of more than 100 scientists. More information on the COSMOS survey is available at https://cosmos.astro.caltech.edu/. We thank the anonymous referee for the careful reading and the useful comments which helped to improve the quality of the paper. We thank Micol Bolzonella and John R. Weaver for the useful suggestions. L.M. acknowledges the support from the grants ASI n.2018-23-HH.0 and PRIN-MUR 2022 20227RNLY3 "The concordance cosmological model: stress-tests with galaxy clusters" supported by Next Generation EU. G.C. acknowledges the support from the grant ASI n.2018-23-HH.

References

Abril-Melgarejo, V., Epinat, B., Mercier, W., et al. 2021, A&A, 647, A152
Aihara, H., AlSayyad, Y., Ando, M., et al. 2019, PASJ, 71, 114
Aihara, H., AlSayyad, Y., Ando, M., et al. 2022, PASJ, 74, 247
Alberts, S., Pope, A., Brodwin, M., et al. 2016, ApJ, 825, 72
Allen, S. W., Evrard, A. E., & Mantz, A. B. 2011, ARA&A, 49, 409
Arnouts, S., Moscardini, L., Vanzella, E., et al. 2002, MNRAS, 329, 355
Bacon, R., Accardo, M., Adjali, L., et al. 2010, in Ground-based and Airborne Instrumentation for Astronomy III, eds. I. S. McLean, S. K. Ramsay, & H. Takami, SPIE Conf. Ser., 7735, 773508
Balogh, M. L., McGee, S. L., Mok, A., et al. 2014, MNRAS, 443, 2679
Bellagamba, F., Maturi, M., Hamana, T., et al. 2011, MNRAS, 413, 1145
Bellagamba, F., Roncarelli, M., Maturi, M., & Moscardini, L. 2018, MNRAS, 473, 5221
Bellagamba, F., Sereno, M., Roncarelli, M., et al. 2019, MNRAS, 484, 1598
Bertin, E., & Arnouts, S. 1996, A&AS, 117, 393
Bleem, L. E., Stalder, B., de Haan, T., et al. 2015, ApJS, 216, 27
Böhringer, H., Schuecker, P., Guzzo, L., et al. 2004, A&A, 425, 367
Brammer, G. B., van Dokkum, P. G., & Coppi, P. 2008, ApJ, 686, 1503
Brodwin, M., Stanford, S. A., Gonzalez, A. H., et al. 2013, ApJ, 779, 138
Cappelluti, N., Brusa, M., Hasinger, G., et al. 2009, A&A, 497, 635
Castignani, G., & Benoist, C. 2016, A&A, 595, A111
Castignani, G., Chiaberge, M., Celotti, A., Norman, C., & De Zotti, G. 2014, ApJ, 792, 114
Castignani, G., Radovich, M., Combes, F., et al. 2022, A&A, 667, A52
Castignani, G., Radovich, M., Combes, F., et al. 2023, A&A, 672, A139
Civano, F., Marchesi, S., Comastri, A., et al. 2016, ApJ, 819, 62
Coil, A. L., Blanton, M. R., Burles, S. M., et al. 2011, ApJ, 741, 8
Comparat, J., Richard, J., Kneib, J.-P., et al. 2015, A&A, 575, A40
Cool, R. J., Moustakas, J., Blanton, M. R., et al. 2013, ApJ, 767, 118
Costanzi, M., Rozo, E., Simet, M., et al. 2019, MNRAS, 488, 4779
Coupon, J., Czakon, N., Bosch, J., et al. 2018, PASJ, 70, S7
Cucciati, O., Lemaux, B. C., Zamorani, G., et al. 2018, A&A, 619, A49
Damjanov, I., Zahid, H. J., Geller, M. J., Fabricant, D. G., & Hwang, H. S. 2018, ApJS, 234, 21
Darvish, B., Mobasher, B., Sobral, D., et al. 2016, ApJ, 825, 113
de Jong, J. T. A., Verdoes Kleijn, G. A., Erben, T., et al. 2017, A&A, 604, A134
De Lucia, G., Springel, V., White, S. D. M., Croton, D., & Kauffmann, G. 2006, MNRAS, 366, 499
DESI Collaboration (Adame, A. G., et al.) 2023, AJ, submitted [arXiv:2306.06308]
Dressler, A. 1980, ApJ, 236, 351
Elvis, M., Civano, F., Vignali, C., et al. 2009, ApJS, 184, 158
Epinat, B. 2021, Extragalactic Spectroscopic Surveys: Past, Present and Future of Galaxy Evolution (GALSPEC2021), 77
Epinat, B., Contini, T., Mercier, W., et al. 2024, A&A, 683, A205
Euclid Collaboration (Adam, R., et al.) 2019, A&A, 627, A23
Farrens, S., Abdalla, F. B., Cypriano, E. S., Sabiu, C., & Blake, C. 2011, MNRAS, 417, 1402
Finoguenov, A., Guzzo, L., Hasinger, G., et al. 2007, ApJS, 172, 182
Finoguenov, A., Watson, M. G., Tanaka, M., et al. 2010, MNRAS, 403, 2063
Gaia Collaboration (Brown, A. G. A., et al.) 2018, A&A, 616, A1
George, M. R., Leauthaud, A., Bundy, K., et al. 2011, ApJ, 742, 125
Giocoli, C., Marulli, F., Moscardini, L., et al. 2021, A&A, 653, A19
Gonzalez, A. 2014, Building the Euclid Cluster Survey – Scientific Program, 7
Gould, K. M. L., Brammer, G., Valentino, F., et al. 2023, AJ, 165, 248
Gozaliasl, G., Finoguenov, A., Tanaka, M., et al. 2019, MNRAS, 483, 3545
Hamana, T., Shirasaki, M., & Lin, Y.-T. 2020, PASJ, 72, 78
Hasinger, G., Cappelluti, N., Brunner, H., et al. 2007, ApJS, 172, 29
Hasinger, G., Capak, P., Salvato, M., et al. 2018, ApJ, 858, 77
Hennig, C., Mohr, J. J., Zenteno, A., et al. 2017, MNRAS, 467, 4015
Hilton, M., Hasselfield, M., Sifón, C., et al. 2018, ApJS, 235, 20
Holden, B. P., Stanford, S. A., Eisenhardt, P., & Dickinson, M. 2004, AJ, 127, 2484
Hung, C.-L., Casey, C. M., Chiang, Y.-K., et al. 2016, ApJ, 826, 130
Ilbert, O., Arnouts, S., McCracken, H. J., et al. 2006, A&A, 457, 841
Ilbert, O., Capak, P., Salvato, M., et al. 2009, ApJ, 690, 1236
Ilbert, O., McCracken, H. J., Le Fèvre, O., et al. 2013, A&A, 556, A55
Ingoglia, L., Covone, G., Sereno, M., et al. 2022, MNRAS, 511, 1484
Iovino, A., Petropoulou, V., Scodeggio, M., et al. 2016, A&A, 592, A78
Kashino, D., Silverman, J. D., Sanders, D., et al. 2019, ApJS, 241, 10
Knobel, C., Lilly, S. J., Iovino, A., et al. 2009, ApJ, 697, 1842
Knobel, C., Lilly, S. J., Iovino, A., et al. 2012, ApJ, 753, 121
Koekemoer, A. M., Aussel, H., Calzetti, D., et al. 2007, ApJS, 172, 196
Koester, B. P., McKay, T. A., Annis, J., et al. 2007, ApJ, 660, 239
Kotulla, R., Fritze, U., Weilbacher, P., & Anders, P. 2009, MNRAS, 396, 462
Kroupa, P. 2002, Science, 295, 82
Kuchner, U., Ziegler, B., Verdugo, M., Bamford, S., & Häußler, B. 2017, A&A, 604, A54
Laigle, C., McCracken, H. J., Ilbert, O., et al. 2016, ApJS, 224, 24
Laigle, C., Pichon, C., Arnouts, S., et al. 2018, MNRAS, 474, 5437
Lang, D., Hogg, D. W., & Mykytyn, D. 2016, Astrophysics Source Code Library [record ascl:1604.008]
Laureijs, R., Amiaux, J., Arduini, S., et al. 2011, ArXiv e-prints [arXiv:1110.3193]
Leauthaud, A., Finoguenov, A., Kneib, J.-P., et al. 2010, ApJ, 709, 97
Lesci, G. F., Marulli, F., Moscardini, L., et al. 2022a, A&A, 659, A88
Lesci, G. F., Nanni, L., Marulli, F., et al. 2022b, A&A, 665, A100
Lilly, S. J., Le Fèvre, O., Renzini, A., et al. 2007, ApJS, 172, 70
Mamon, G. A., Biviano, A., & Boué, G. 2013, MNRAS, 429, 3079
Marulli, F., Veropalumbo, A., Sereno, M., et al. 2018, A&A, 620, A1
Masters, D. C., Stern, D. K., Cohen, J. G., et al. 2019, ApJ, 877, 81
Maturi, M., Meneghetti, M., Bartelmann, M., Dolag, K., & Moscardini, L. 2005, A&A, 442, 851
Maturi, M., Bellagamba, F., Radovich, M., et al. 2019, MNRAS, 485, 498
McCracken, H. J., Milvang-Jensen, B., Dunlop, J., et al. 2012, A&A, 544, A156
Moneti, A., McCracken, H. J., Hudelot, W., et al. 2023, VizieR Online Data Catalog: II/373
Navarro, J. F., Frenk, C. S., & White, S. D. M. 1997, ApJ, 490, 493
Paulino-Afonso, A., Sobral, D., Darvish, B., et al. 2018, A&A, 620, A186
Postman, M., Lubin, L. M., Gunn, J. E., et al. 1996, AJ, 111, 615
Pratt, G. W., Arnaud, M., Biviano, A., et al. 2019, Space Sci. Rev., 215, 25
Puddu, E., Radovich, M., Sereno, M., et al. 2021, A&A, 645, A9
Radovich, M., Tortora, C., Bellagamba, F., et al. 2020, MNRAS, 498, 4303
Ramella, M., Boschin, W., Fadda, D., & Nonino, M. 2001, A&A, 368, 776
Romanello, M., Marulli, F., Moscardini, L., et al. 2024, A&A, 682, A72
Rosani, G., Caminha, G. B., Caputi, K. I., & Deshmukh, S. 2020, A&A, 633, A159
Rosati, P., Borgani, S., & Norman, C. 2002, ARA&A, 40, 539
Rozo, E., Wechsler, R. H., Rykoff, E. S., et al. 2010, ApJ, 708, 645
Rykoff, E. S., Rozo, E., Busha, M. T., et al. 2014, ApJ, 785, 104
Sarron, F., & Conselice, C. J. 2021, MNRAS, 506, 2136
Schechter, P. 1976, ApJ, 203, 297
Scoville, N., Aussel, H., Brusa, M., et al. 2007, ApJS, 172, 1
Sereno, M. 2016, MNRAS, 455, 2149
Singh, P., Saro, A., Costanzi, M., & Dolag, K. 2020, MNRAS, 494, 3728
Skelton, R. E., Bell, E. F., & Somerville, R. S. 2012, ApJ, 753, 44
Smolčić, V., Schinnerer, E., Finoguenov, A., et al. 2007, ApJS, 172, 295
Smolčić, V., Novak, M., Bondi, M., et al. 2017, A&A, 602, A1
Stapelberg, S., Carrasco, M., & Maturi, M. 2019, MNRAS, 482, 1824
Story, K. T., Reichardt, C. L., Hou, Z., et al. 2013, ApJ, 779, 86
Strazzullo, V., Daddi, E., Gobat, R., et al. 2016, ApJ, 833, L20
Sunyaev, R. A., & Zeldovich, Y. B. 1970, Comments Astrophys. Space Phys., 2, 66
Taamoli, S., Mobasher, B., Chartab, N., et al. 2024, ApJ, 966, 18
Taniguchi, Y., Kajisawa, M., Kobayashi, M. A. R., et al. 2015, PASJ, 67, 104
The Dark Energy Survey Collaboration 2005, arXiv e-prints [arXiv:astro-ph/0510346]
To, C., Krause, E., Rozo, E., et al. 2021, Phys. Rev. Lett., 126, 141301
van der Wel, A., Bezanson, R., D'Eugenio, F., et al. 2021, ApJS, 256, 44
Veropalumbo, A., Marulli, F., Moscardini, L., Moresco, M., & Cimatti, A. 2014, MNRAS, 442, 3275
Vikhlinin, A., McNamara, B. R., Forman, W., et al. 1998, ApJ, 502, 558
Vikhlinin, A., Kravtsov, A. V., Burenin, R. A., et al. 2009, ApJ, 692, 1060
Weaver, J. R., Kauffmann, O. B., Ilbert, O., et al. 2022, ApJS, 258, 11
Weaver, J. R., Zalesky, L., Kokorev, V., et al. 2023, ApJS, 269, 20
Zamojski, M. A., Schiminovich, D., Rich, R. M., et al. 2007, ApJS, 172, 468
Zatloukal, M., Röser, H. J., Wolf, C., Hippelein, H., & Falter, S. 2007, A&A, 474, L5
Zenteno, A., Mohr, J. J., Desai, S., et al. 2016, MNRAS, 462, 830